*Acta Oceanol. Sin.*, 2023, Vol. 42, No. 10, P. 23–35
https://doi.org/10.1007/s13131-023-2251-1
http://www.aosocean.com
E-mail: ocean2@hyxb.org.cn

# Cross-shelf variation of internal tides west of the Dongsha Plateau in the northern South China Sea

Wei Yang[1, 2, 3, 4], Ruixiang Li[3, 4], Yanqing Feng[3, 4], Huijie Xue[5]*

[1] State Key Laboratory of Tropical Oceanography, South China Sea Institute of Oceanology, Chinese Academy of Sciences, Guangzhou 510301, China

[2] University of Chinese Academy of Sciences, Beijing 100049, China

[3] South China Sea Marine Survey Center, Ministry of Natural Resources, Guangzhou 510300, China

[4] Key Laboratory of Marine Environment Survey Technology and Application, Ministry of Natural Resources, Guangzhou 510300, China

[5] State Key Laboratory of Marine Environmental Science, Xiamen University, Xiamen 361102, China

Received 27 February 2023; accepted 12 May 2023



**Abstract**

We examine the cross-shelf variation of internal tides (ITs) west of the Dongsha Plateau in the northern South China Sea based on observations from 4 moorings deployed between August 2017 and September 2018. On the slope, the amplitude of diurnal baroclinic current ellipses are 5 times larger than that of barotropic currents. The baroclinic energy quickly dissipates during cross-shelf propagation, and barotropic currents become dominant on the shelf outside of the Zhujiang River Estuary, with the amplitude of semidiurnal barotropic current ellipses being 10 times larger than that of the baroclinic ones. Dynamic modal decomposition indicates the first baroclinic mode is dominant for both diurnal and semidiurnal ITs. The total horizontal kinetic energy (HKE) of the first three baroclinic modes shows spatiotemporal differences among the 4 moorings. On the slope, the HKE for diurnal ITs is stronger in summer and winter, but weaker in spring and autumn; for semidiurnal ITs there is a similar seasonal variation, but the HKE in winter is even stronger than that in summer. On the shallow shelf, both diurnal and semidiurnal ITs maintain a certain intensity in summer but almost disappear in winter. Further analysis shows that only the upper water column is affected by seasonal variation of stratification on the slope, variation of diurnal ITs is thus controlled by the semi-annual cycle of barotropic energy input from the Luzon Strait, while the incoherent baroclinic currents make a major contribution to the temporal variation of semidiurnal ITs. For the shelf region, the water column is well mixed in winter, and the baroclinic energy largely dissipates when ITs propagate to the shelf zone despite of a strong barotropic energy input from the Luzon Strait .

**Key words:** internal tide, Dongsha Plateau, cross-shelf variation, dynamic modal decomposition, coherent

**Citation:** Yang Wei, Li Ruixiang, Feng Yanqing, Xue Huijie. 2023. Cross-shelf variation of internal tides west of the Dongsha Plateau in the northern South China Sea. Acta Oceanologica Sinica, 42(10): 23–35, doi: 10.1007/s13131-023-2251-1

## 1 Introduction

An internal tide (IT) is an internal gravity wave that is generated at a tidal frequency by the interaction of barotropic tidal flow with abrupt bottom topography in a stratified ocean (Niwa and Hibiya, 2001; Garrett and Kunze, 2007). In contrast to surface tides, ITs have large-amplitude pycnocline oscillations accompanied by depth-varying currents and are characterized by relatively short horizontal wavelengths on the order of 100 km (Niwa and Hibiya, 2004; Jan et al., 2007). After their generation, high-mode ITs usually break and dissipate near their source regions and thus enhance local mixing (St. Laurent and Garrett, 2002; Tian et al., 2006, 2009; Klymak et al., 2011), and may also lead to along-slope near-bottom transport (Xie et al., 2018), whereas low-mode ITs may propagate thousands of kilometers (Alford, 2003; Rainville and Pinkel, 2006; Xu et al., 2016). During their long-range propagation through complex background conditions and variable stratification, ITs may lose coherence to the astronomical tides and show incoherent characteristics (Eich et al., 2004; Park et al., 2006; Cao et al., 2017).

When barotropic tidal currents flow over the Luzon Strait (LS), which is featured by two north-south oriented ridges, strong ITs are generated, making the South China Sea (SCS) one of the most energetic regions of ITs in the world (Duda et al., 2004; Alford et al., 2015); the observed baroclinic current and vertical displacement in the LS can exceed 2 m/s and 300 m, respectively (Alford et al., 2011). Numerical experiments show that about 25% of $M_2$ (14 GW in 56 GW, Niwa and Hibiya, 2004) and 36% of $K_1$ (12.4 GW in 34.2 GW, Jan et al., 2007) barotropic tidal energy are converted to baroclinic energy in the LS. About half of the generated baroclinic tidal energy dissipates locally, while the rest radiates westward into the SCS and eastward into the western Pacific (Jan et al., 2008; Xu et al., 2016). The ITs in the SCS mostly are radiated from the LS, which propagate westward across the deep central basin before arriving in the slope area around the Dong-

Foundation item: The Key-Area Research and Development Project of Guangdong Province under contract No. 2020B1111020003; the Science and Technology Plan Projects of Guangdong Province under contract No. 2021B1212050025; the Science and Technology Development Fund of the South China Sea Bureau, Ministry of Natural Resources under contract No. 202205.
*Corresponding author, E-mail: hjxue@xmu.edu.cn

sha Plateau (DP), where they further steepen into internal solitary waves (ISWs) and finally dissipate over the shallow shelf zone outside of the Zhujiang River Estuary (ZRE; Ramp et al., 2004; Lien et al., 2005; Farmer et al., 2009; Alford et al., 2015). Recent studies have also revealed that low-mode ITs originating from the LS can even propagate far enough to arrive at the Vietnam coast and Nansha Islands that are more than 1 000-1 500 km away (Zhao, 2014; Xu et al., 2016; Liu et al., 2016). Baroclinic energy input from the LS is thought to be the main reason for the temporal variation of ITs in the northern SCS (Xu et al., 2014; Cao et al., 2017). Recent studies show that the background currents associated with Kuroshio intrusion and mesoscale eddies are also important for modulating internal tidal currents. The radiating tidal pattern and energy dissipation of ITs respond differently to different Kuroshio paths in the LS (Xu et al., 2021), and the propagation speed and energy conversion of semidiurnal ITs can be modulated by mesoscale eddies (Huang et al., 2018), and further become incoherent (Li et al., 2020).

Many studies have addressed temporal variations of ITs in oceans around the world, such as the North American coast (Kelly et al., 2012), the northwest shelf of Australia (Holloway et al., 2001), and the west coast of India (Subeesh and Unnikrishnan, 2016). Since the Asian Seas International Acoustics Experiment (ASIAEX) in 2001, the ITs in the northern SCS have been extensively surveyed based on long-term field observations (Guo et al., 2012; Ma et al., 2013; Xu et al., 2013, 2014; Liu et al., 2015; Cao et al., 2017; Chen et al., 2019; Li et al., 2020; Fig. 1). Diurnal ITs dominant over semidiurnal ITs in the northern SCS (Duda et al., 2004; Duda and Rainville, 2008; Xu et al., 2013). Diurnal ITs are stronger in summer and winter but weaker in spring and autumn in the LS (Xu et al., 2014; Liu et al., 2015) and the adjacent SCS deep basin (Cao et al., 2017; Li et al., 2020). For the region northeast of the DP, the observed diurnal ITs are also stronger in summer and winter at deep water moorings, while less seasonal variation is found on the shallow shelf (Ma et al., 2013; Chen et al., 2019). For the region west of the DP, Xu et al. (2013) analyse a 9-month data set and mention that diurnal ITs are strongest in summer, but weakest in winter. Compared with diurnal ITs, Xu et al. (2014) indicate that semidiurnal ITs are seasonally invariant in the LS, while Cao et al. (2017) find that strong semidiurnal ITs always appear in spring and autumn, and the seasonal variation of semidiurnal ITs is also irregular in the slope region around the DP (Ma et al., 2013; Chen et al., 2019).

Therefore, relatively consistent conclusions have been reached for the temporal variations of ITs from the LS to the region east of the DP in the northern SCS, indicating that diurnal ITs are stronger in summer and winter than that in spring and autumn, whereas the seasonal variation of semidiurnal ITs is irregular. In contrast, much less attention has been paid to the region west of the DP with scanty *in situ* observations. Furthermore, previous studies have focused mainly on the longitudinal variation of ITs in the northern SCS, although Guo et al. (2012) emphasize that the intensity of internal tidal flow decreases significantly when ITs propagate from the deeper shelf break to the shallower shelf in winter, but the authors do not mention ITs in summer. Cross-shelf variation of ITs requires further study. Based on observations from 4 moorings deployed between August 2017 and September 2018, this study examines the cross-shelf variation of ITs and discusses the factors controlling the temporal variation of diurnal and semidiurnal ITs in the slope-shelf area west of the DP. This paper is organized as follows. Section 2 describes the field observations and methods. The cross-shelf characteristics of barotropic and baroclinic currents, along with the dynamic modal structures and seasonal variation of horizontal kinetic energy are presented in Section 3. Discussion of the variation of diurnal and semidiurnal ITs is given in Section 4, and a summary follows in Section 5.

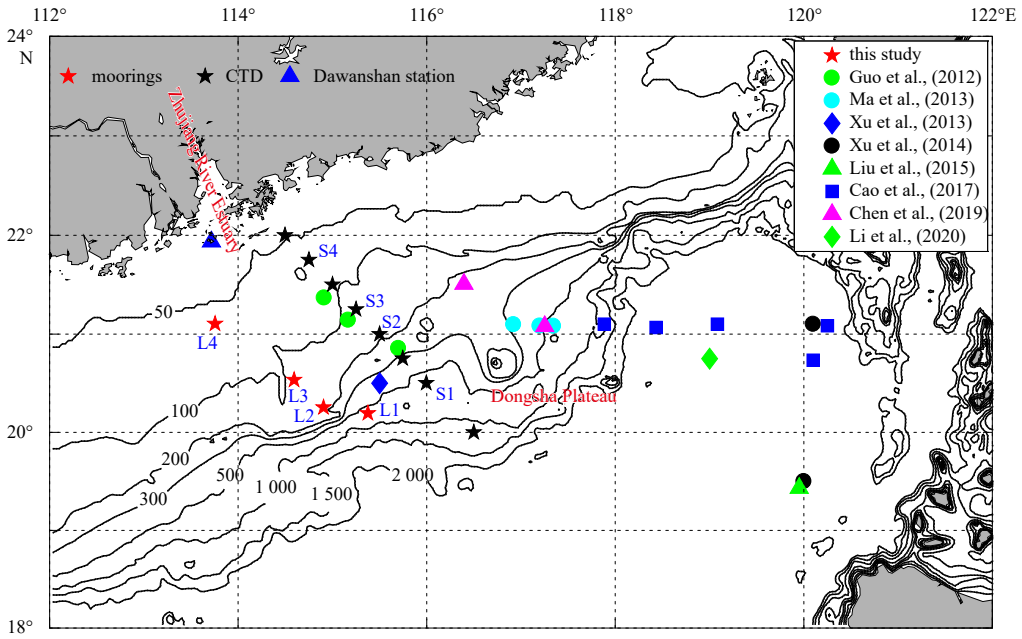


**Fig. 1.** Sampling locations of four current moorings (L1–L4, red stars), seasonal CTD observation section (black stars; S1–S4 are indicated), and Dawanshan gauge station (blue triangle) in the northern South China Sea. Mooring locations from recent studies for the temporal variations of internal tides between the Luzon Strait and the Zhujiang River Estuary are also indicated (note that only moorings with an observation period of more than 3 months are shown here). The bathymetry (black line contours, unit: m) is taken from Etopo2.

## 2 Data and methods

### 2.1 *Field observations*

Four moored acoustic Doppler current profilers (ADCPs, named L1–L4) were deployed on the slope-shelf area west of the DP during 2017–2018, covering a distance of ~200 km in the cross-shelf direction with a depth range from 546 m to 76 m. L1 was located on the slope where the bathymetry rapidly changed between 500 m and 1 000 m, while L2–L4 were located on the relatively flat shelf where the water column depth was less than 200 m (Fig. 1). L1 (L2) was equipped with two 150 (300) kHz ADCPs, one looking upward and the other downward, at a nominal depth of ~250 m (~70 m). L3 (L4) was equipped with one 300 kHz looking upward and one 600 kHz ADCP looking downward at a nominal depth of ~90 m (~55 m). The sample interval and bin size were 3 min and 8 m for 150 kHz, 10 min and 4 m for 300 kHz, and 10 min and 2 m for 600 kHz ADCPs. The effective ranges of current observations for L1 to L4 were 34–522 m, 17–176 m, 11–110 m, and 16–67 m, respectively, which covered 89%, 85%, 87%, and 68% of the whole water column, with corresponding observed durations of 266 d, 376 d, 241 d, and 115 d (Table 1). Careful quality control was conducted; raw data were directly abandoned in cases that the velocity exceeded 3 m/s or good percentage (PG1+PG4, output from ADCP for quality assessment of raw current data) less than 50%, the data gaps were filled with linear interpolation, and the current data were smoothed hourly for IT analysis.

In order to obtain seasonal stratification conditions in the northern SCS, *in situ* data from a cross-shelf hydrographic section consisting of 8 Conductivity-Temperature-Depth (CTD) stations were collected. This hydrographic section was basically parallel to the mooring line and located about 100 km to the east (Fig. 1). Temperature, conductivity, and depth were measured by SBE 911 plus CTD (SEA-BIRD ELECTRONICS INC., USA), and the raw data were saved at 1 m intervals after quality control for analysis. The hydrographic cruises were conducted on 13 August 2017, 17 November 2017, 31 January 2018, and 13 May 2018, and the water depths of S1–S4 were similar to those of L1–L4. Meanwhile the tidal level at Dawanshan gauge station (21°56′N, 113°43′E) was also collected to obtain astronomical tide variation on the shelf outside of the ZRE during the observation period.

### 2.2 *Harmonic analysis and band-pass filtering of internal tides*

The barotropic current is defined as the depth-integrated flow, and the baroclinic current is the residual once the barotropic current is removed. A MATLAB-based package applying a least-squares fit method is used to characterize the principal tidal constituents for both barotropic and baroclinic currents (Pawlowicz et al., 2002). To extract the diurnal and semidiurnal tidal currents, a fourth-order Butterworth filter is applied to the baroclinic currents, and the cutoff frequencies ($f$) for the diurnal and semidiurnal bands are set at $0.9f_{O_1}-1.1f_{K_1}$ (i.e., 0.84–1.10 cycles per day (cpd)) and $0.9f_{M_2}-1.1f_{S_2}$ (i.e., 1.74–2.20 cpd) respectively.

### 2.3 *Rotary spectra*

Rotary spectra can be used to describe the rotational components of currents at various frequencies. In this study, the total energy spectra of the barotropic currents, including the counterclockwise and clockwise rotary components, are presented to characterize the spectra density at the diurnal and semidiurnal frequency bands.

### 2.4 *Dynamic modal decomposition*

In an idealized ocean with a constant water depth $H$, ITs can be described by a superposition of discrete baroclinic modes, which depend on the buoyancy frequency profile $N(z)$. The baroclinic modes for vertical displacement $\Phi(z)$ can be determined by the following equation:

$$\frac{\mathrm{d}^2\Phi(z)}{\mathrm{d}z^2}+\frac{N^2(z)}{C_n^2}\Phi(z)=0, \tag{1}$$

with the boundary conditions $\Phi(0)=\Phi(H)=0$ (the rigid lid approximation), where $n$ is the mode number, and $C_n$ is the eigen speed (Gill, 1982).

The corresponding baroclinic modes for pressure and horizontal velocity $\Pi(z)$ are related to $\Phi(z)$ via

$$\Pi(z)=\rho_0 C_n^2\frac{\mathrm{d}\Phi(z)}{\mathrm{d}z}, \tag{2}$$

where $\rho_0$ is the water density (Zhao et al., 2010). The baroclinic velocity of Mode-$n$ can be expressed as

$$u_n'(z,t)=u_n'(t)\,\Pi_n(z), \tag{3}$$

where $u_n'(t)$ represents the time-varying magnitudes of the baroclinic Mode-$n$, which can be extracted from the observed velocity profile by least-squares modal fitting at each time point (Alford, 2003; Nash et al., 2005; Shang et al., 2015), and $\Pi_n(z)$ is the normalized vertical structure of baroclinic Mode-$n$, which can be calculated from Eqs (1) and (2) with the buoyancy frequency profile $N(z)$. The CTD profiles of S1–S4 during the observation are used for calculating the buoyancy frequency at the mooring L1–L4. In this study, the observed ITs are dominated by lower modes, which will be shown in Section 3.3. Therefore, only the first three baroclinic modes are extracted in the modal decomposition. The buoyancy frequency profiles in four seasons and the corresponding vertical structures of the first three baroclinic modes for the horizontal velocity are presented in Fig. 2. Then the modal fitted perturbation $u_n'(z,t)$ can be calculated from Eq. (3). Finally, the depth-integrated horizontal kinetic energy (HKE) of Mode-$n$ ($n$ = 1, 2, 3) is computed from $u_n'(z,t)$ as

$$\mathrm{HKE}=\frac{1}{2}\rho_0\int_{-H}^{0}\left\langle\left|u_n'(z,t)\right|^2\right\rangle\mathrm{d}z, \tag{4}$$

**Table 1.** Location, depth, date range, record length, instrument, and sample depth of moorings at L1–L4

| Station | Latitude | Longitude | Depth/m | Date Range | Record length/d | Instrument | Sample depth/m |
|---|---|---|---|---|---|---|---|
| L1 | 20°11′43.08″N | 115°22′37.50″E | 546 | 2018.01.07–2018.09.30 | 266 | 150 kHz ADCP×2 | 34–522 |
| L2 | 20°15′14.34″N | 114°54′24.12″E | 186 | 2017.08.31–2018.04.23<br>2018.05.12–2018.09.30 | 376 | 300 kHz ADCP×2 | 17–176 |
| L3 | 20°32′04.14″N | 114°35′39.18″E | 114 | 2017.08.31–2017.12.11<br>2018.03.19–2018.08.05 | 241 | 300&600 kHz ADCP | 11–110 |
| L4 | 21°06′16.02″N | 113°45′20.64″E | 76 | 2018.01.07–2018.03.19<br>2018.06.23–2018.08.06 | 115 | 300&600 kHz ADCP | 16 –67 |

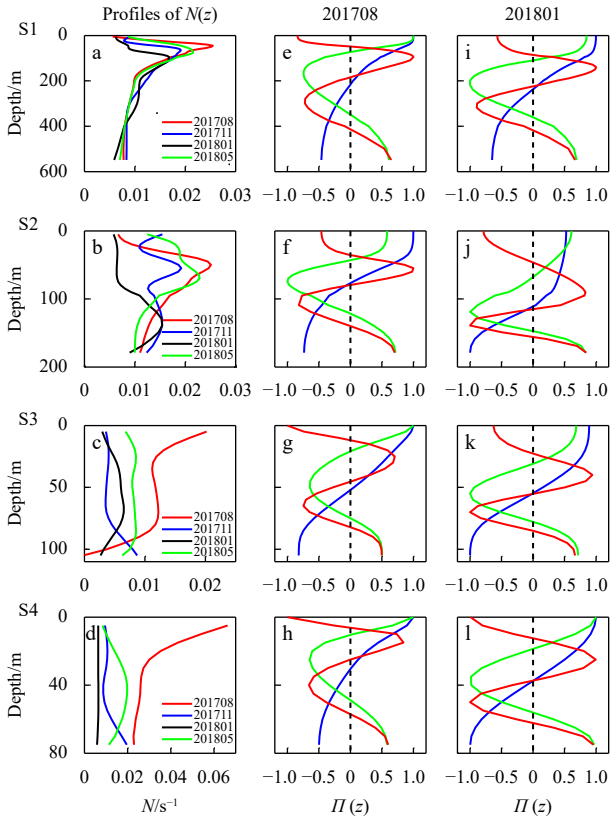


**Fig. 2.** Buoyancy frequency profiles of S1–S4 (a–d) and the corresponding normalized vertical structures of the first three baroclinic modes (the blue, green and red lines stand for Modes 1–3) for the horizontal velocity in August 2017 (e–h) and January 2018 (i–l).

where the angle bracket indicates the average over one tidal cycle (Shang et al., 2015; Liu et al., 2019).

### 2.5 *Calculation of coherent and incoherent motions*

Based on a least-squares fit of harmonic analysis, the diurnal and semidiurnal coherent ITs can be obtained by

$$u_{\mathrm{C}} = \sum_{n} U_n \cos(\psi_n + \omega_n t), \tag{5}$$

where $U_n$ is the amplitude, $\psi_n$ is the phase, and $\omega_n$ is the frequency of the principal tidal constituents. The $K_1$, $O_1$, $P_1$, $Q_1$ ($M_2$, $S_2$, $N_2$, $K_2$) tidal constituents are chosen for the coherent diurnal (semidiurnal) ITs calculation.

$$u_{\mathrm{IC}} = u_{\mathrm{bandpass}} - u_{\mathrm{C}}. \tag{6}$$

The residual currents containing incoherent ITs are obtained by subtracting the coherent ITs from the band-passed baroclinic currents (van Haren, 2004; Xie et al., 2013; Liu et al., 2016).

## 3 Results

### 3.1 *Barotropic tidal currents*

Barotropic currents are essential for extracting baroclinic currents. There are two main methods for barotropic current calculation; one directly from the depth-integrated flow, which requires observations from the whole depth and is relatively easy to carry out on the slope. The so-calculated barotropic tidal ellipses in the slope-shelf area northeast of the DP (Beardsley et al., 2004) have been widely used to validate IT numerical models (Jan et al., 2007; Xu et al., 2016). The second method is obtained from the global tidal model. Previous studies have shown that barotropic tidal currents extracted from TOPEX/Poseidon Global Inverse Solution developed by Oregon State University (Egbert and Erofeeva, 2002) agree well with the observed barotropic currents in the northern SCS (Ramp et al., 2004; Alford et al., 2011), and thus this method is widely used for baroclinic current extraction in the deep basin (Xu et al., 2014; Cao et al., 2017; Huang et al., 2018; Zhai et al., 2020).

The observed ranges of ADCPs cover more than 85% of the entire water depth except for L4 (68%), and the barotropic currents are directly calculated from the depth-integrated flow in this study. Figure 3a shows the barotropic tidal ellipses of the

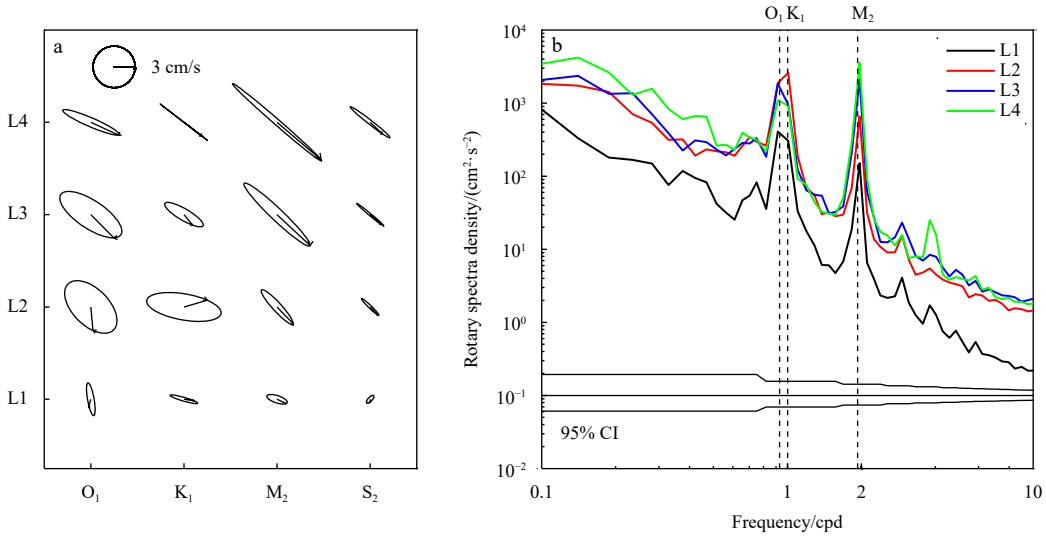


**Fig. 3.** Barotropic tidal ellipses for the principal constituents ($O_1$, $K_1$, $M_2$, and $S_2$) (a) and rotary spectra density of barotropic currents at L1–L4 (b). The arrows in a denote the rotation directions of the ellipses, the lines from the center show the Greenwich phases, and the upper-left icon is the current scale for the axes. cpd: cycles per day.

dominant diurnal $K_1$ and $O_1$ constituents and the semidiurnal $M_2$ and $S_2$ constituents. For the $K_1$ constituent, the current amplitude is smallest, 2.0 cm/s, at L1, which is located on the slope; it increases to 5.4 cm/s at L2 on the shelf, and then gradually decreases at L4; and for the $O_1$ constituent, the current amplitude is smallest, 2.4 cm/s, at L1, it increases to 5.2 cm/s at L3, and then gradually decreases at L4 (Table 2). The two diurnal tidal constituents are generally comparable in this area, and $O_1$ is even stronger than $K_1$ on the shallow shelf. For the two semidiurnal constituents, the tidal currents of $M_2$ are obviously stronger than those of $S_2$. For the $M_2$ ($S_2$) constituent, the current amplitude is smallest, 1.5 cm/s (0.7 cm/s), on the slope and then monotonically increases to a maximum of 8.5 cm/s (3.6 cm/s) on the shallow shelf (Table 2). The ellipse orientations are almost along the cross-shelf direction, especially for sites on the shelf. Figure 3b shows the rotary spectral density of the barotropic currents at L1–L4, which is characterized by two peaks in the diurnal and semidiurnal frequency bands. The diurnal tidal energy is stronger than the semidiurnal tidal energy at L1 and L2, and vice versa at L3 and L4. The spectra density in the semidiurnal frequency band monotonically increases along the cross-shelf direction from L1 to L4, but for the diurnal frequency band, there are some differences between $O_1$ and $K_1$; the spectra density of the $K_1$ frequency attains a maximum at L2, while for the $O_1$ frequency, the maximum density is at L3.

The distributions of barotropic tidal ellipses in this paper are consistent with results from ASIAEX in 2001 (Beardsley et al., 2004; Duda and Rainville, 2008); both show the current amplitudes of semidiurnal tides monotonically increasing along the cross-shelf direction, while diurnal tides first increase, then decrease when they arrive at the shallow shelf. The current amplitude of $M_2$ is 16.6 cm/s northeast of the DP in ASIAEX (Beardsley et al., 2004), obviously larger than the 8.5 cm/s in this paper. Similarly, the current amplitude of $K_1$ is 11.9 cm/s in ASIAEX (Beardsley et al., 2004), also larger than the 5.4 cm/s in this paper, and this is related to the propagation of barotropic tides originating from the western Pacific and entering the SCS through the LS (Fang et al., 1999), which arrive at the ASIAEX sites prior to the sites of this study.

**Table 2.** Ellipse parameters of the principal diurnal and semidiurnal barotropic tidal constituents

| | Station | Major axis velocity/ (cm·s$^{-1}$) | Minor axis velocity/ (cm·s$^{-1}$) | Ellipse orientation/(°) | Phase/(°) |
|---|---|---|---|---|---|
| $O_1$ | L1 | 2.4 | –0.5 | 100 | 113 |
| | L2 | 4.6 | –2.6 | 134 | 125 |
| | L3 | 5.2 | –2.0 | 146 | 152 |
| | L4 | 4.4 | –0.6 | 156 | 171 |
| $K_1$ | L1 | 2.0 | –0.3 | 164 | 225 |
| | L2 | 5.4 | –1.9 | 170 | 235 |
| | L3 | 3.2 | 0.8 | 150 | 234 |
| | L4 | 4.3 | 0.1 | 142 | 219 |
| $M_2$ | L1 | 1.5 | 0.5 | 162 | 201 |
| | L2 | 3.3 | 0.6 | 132 | 173 |
| | L3 | 6.5 | –0.9 | 136 | 184 |
| | L4 | 8.5 | –0.4 | 139 | 192 |
| $S_2$ | L1 | 0.7 | 0.3 | 47 | 114 |
| | L2 | 1.7 | 0.2 | 136 | 207 |
| | L3 | 2.5 | 0.2 | 140 | 216 |
| | L4 | 3.6 | 0.3 | 142 | 227 |

### 3.2 *Baroclinic tidal currents*

#### 3.2.1 *Band-passed baroclinic currents*

Cross-shelf baroclinic currents (the original velocities are rotated 45° counterclockwise) are band-passed for the diurnal and semidiurnal ITs at L1–L4 (Figs 4 and 5). The time series of observed tidal elevation at Dawanshan gauge station and the predicted elevation containing eight major tidal constituents ($M_2$, $S_2$, $N_2$, $K_2$ and $K_1$, $O_1$, $P_1$, $Q_1$) in the LS (20°N, 122°E) extracted from TPXO 7.2 are also shown.

In July 2018, there are energetic ITs on the slope and shelf area west of the DP, especially for the diurnal frequency. The cross-shelf diurnal baroclinic currents show an apparent fortnightly cycle, like the astronomical tide in Fig. 4a, but there is an obvious time lag between the barotropic tides and the baroclinic currents. Taking the spring tide around 15 July as an example (note the phase of the observed tide at Dawanshan station lags by about 3 h behind the predicted tide in the LS (Fig. 4a), which agrees well with the cotidal charts (about one-quarter of the semidiurnal cycle and one-eighth of the diurnal cycle) from previous studies (Fang et al., 1999; Zu et al., 2008)), the corresponding energetic ITs appear around 18 to 19 July at L1 and L2, from 19 to 20 July at L3, and from 21 to 22 July at L4, which shows a cross-shelf delay. It takes 3 d to 4 d for the energetic ITs to propagate from the LS to the slope area west of the DP, and another 2 d to 3 d from the slope region to the shelf area outside of the ZRE. Diurnal ITs show a notable surface and bottom intensification, with a magnitude of 20–35 cm/s in the upper 100 m and 15–20 cm/s in the bottom 200 m at L1. At L2 and L3, diurnal IT currents with a magnitude of 20 cm/s appear throughout the whole water column and become obviously weaker with a magnitude of less than 10 cm/s at L4. For all four sites, semidiurnal ITs are much weaker than diurnal ITs, and semidiurnal ITs are relatively stronger at L2 and L3, with a magnitude reaching about 20 cm/s in the upper 50 m.

The cross-shelf band-passed baroclinic currents between 10 January and 9 February 2018 are shown in Fig. 5. Generally speaking, diurnal ITs in winter are comparable with those in summer, and semidiurnal ITs are even stronger in winter, especially for the semidiurnal baroclinic currents at L1 and L2 during the spring tide around 20 January. The barotropic tides show an apparent fortnightly cycle in Fig. 5a, but the intensity of the observed baroclinic currents for the two spring-neap cycles are different; the diurnal and semidiurnal baroclinic currents around 16 January are obviously stronger than those around 1 February, and the reason needs further study. For the vertical structure, diurnal ITs at L1 mainly show Mode-1 in winter, although there is a slight Mode-2 structure between 1 and 4 February, and semidiurnal ITs are observed with an apparent Mode-2 structure around 20 January. For L4, located on the shallow shelf outside of the ZRE, the diurnal and semidiurnal baroclinic currents almost completely disappear in winter.

#### 3.2.2 *Baroclinic tidal ellipses*

The baroclinic tidal ellipses of the principal diurnal ($O_1$ and $K_1$) and semidiurnal ($M_2$ and $S_2$) constituents are shown in Fig. 6. At L1, the diurnal tidal currents are intensified at the surface and bottom, with the amplitude of $K_1$ exceeding 13.3 cm/s and 10.5 cm/s near the surface and bottom layers, respectively. The nearly 180° phase difference between the upper and bottom layers indicates a prominent Mode-1 structure with a reversal depth of ~270 m where the amplitude of $K_1$ decreases to 0.9 cm/s. However, for L2, located 50 km northwest of L1, the amplitudes

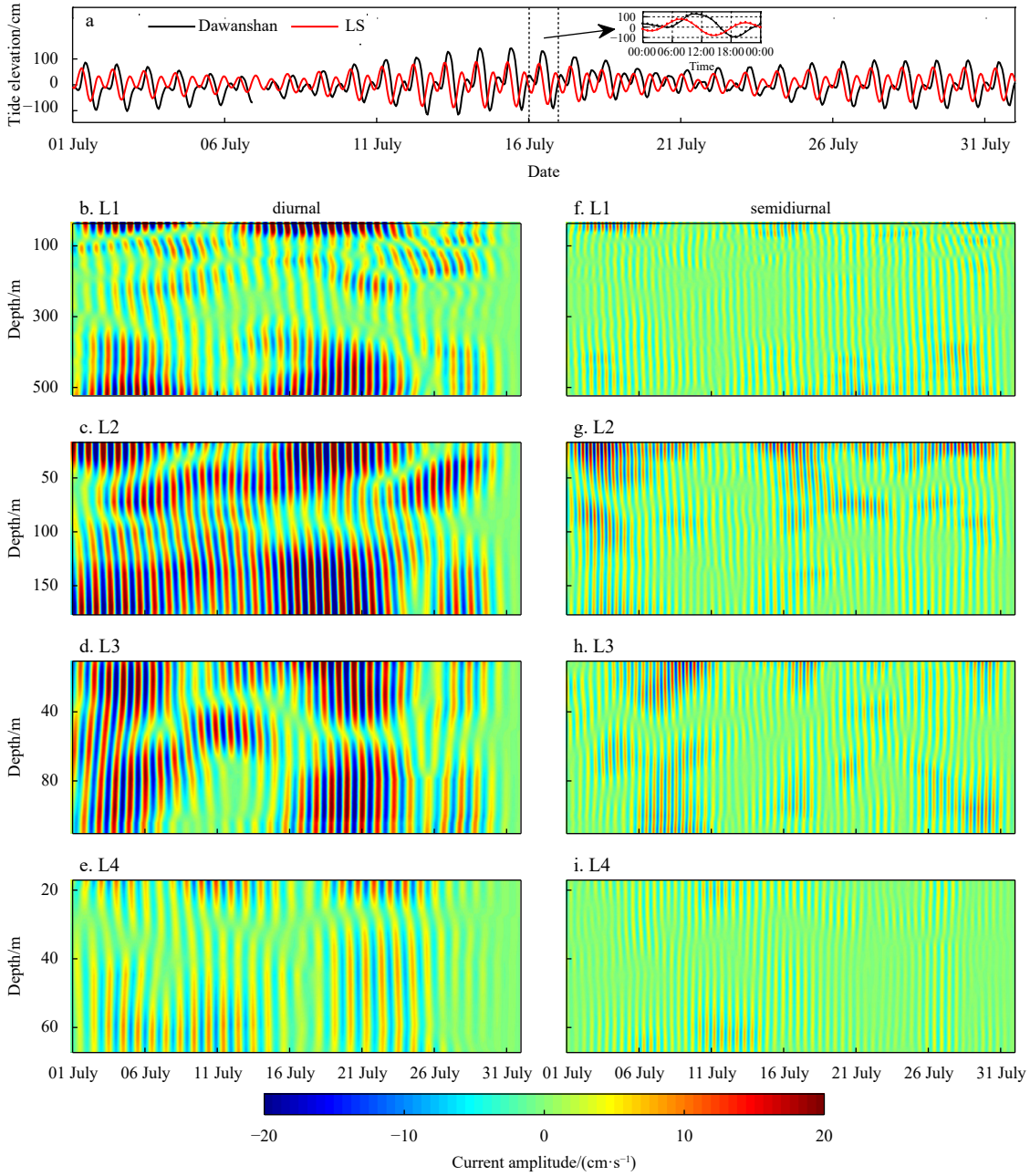


**Fig. 4.** Time series of tidal elevation at Dawanshan gauge station (black line) and the Luzon Strait (LS) (20°N, 122°E; red line) obtained from TPXO 7.2 (a). Band-passed diurnal (b–e) and semidiurnal (f–i) baroclinic cross-shelf currents at L1–L4 in July 2018.

of $K_1$, $O_1$, and $M_2$ become comparable in the upper layers, and the ellipse orientation is along the cross-shelf direction. The diurnal $O_1$ exhibits an obvious Mode-2 structure with two reversal depths at around 65 m and 120 m, while $K_1$ and $M_2$ are still dominantly Mode-1 structure. High-mode ITs tend to dissipate locally, and the appearance of Mode-2 ITs at L2 is probably due to the dissipation of baroclinic energy as strong diurnal ITs propagate across the steep bottom topography between L1 and L2. The diurnal baroclinic currents are also prominently stronger than those of the semidiurnal ITs at L3. $K_1$ and $O_1$ mainly display Mode-1 structure with a reversal depth of around 50 m, and the baroclinic current amplitude of $O_1$ becomes larger than that of $K_1$. For L4 on the shallow shelf, the amplitudes of diurnal baroclinic currents are 2.3 cm/s and 2.8 cm/s at the surface and bottom layers, less than those of barotropic currents, and barotropic currents become dominant with the amplitudes of semidiurnal baroclinic current ellipses being nearly one-tenth of those of the barotropic ones.

### 3.3 *Cross-shelf variation of HKE*

#### 3.3.1 *Dynamic modal structure*

For diurnal ITs, the total depth-integrated kinetic energy (sum of the first three diurnal baroclinic modes) shows an apparent fortnightly spring-neap cycle and the dominant Mode-1 structure at L1 (Fig. 7a). The averaged Mode-1 signal during the whole observation accounts for 75% of the total kinetic energy with a slightly higher percentage of 78% in summer and a relative lower percentage of 54% in winter. Compared with L1, the kinetic energy is largely reduced at L2, and the fortnightly spring-neap

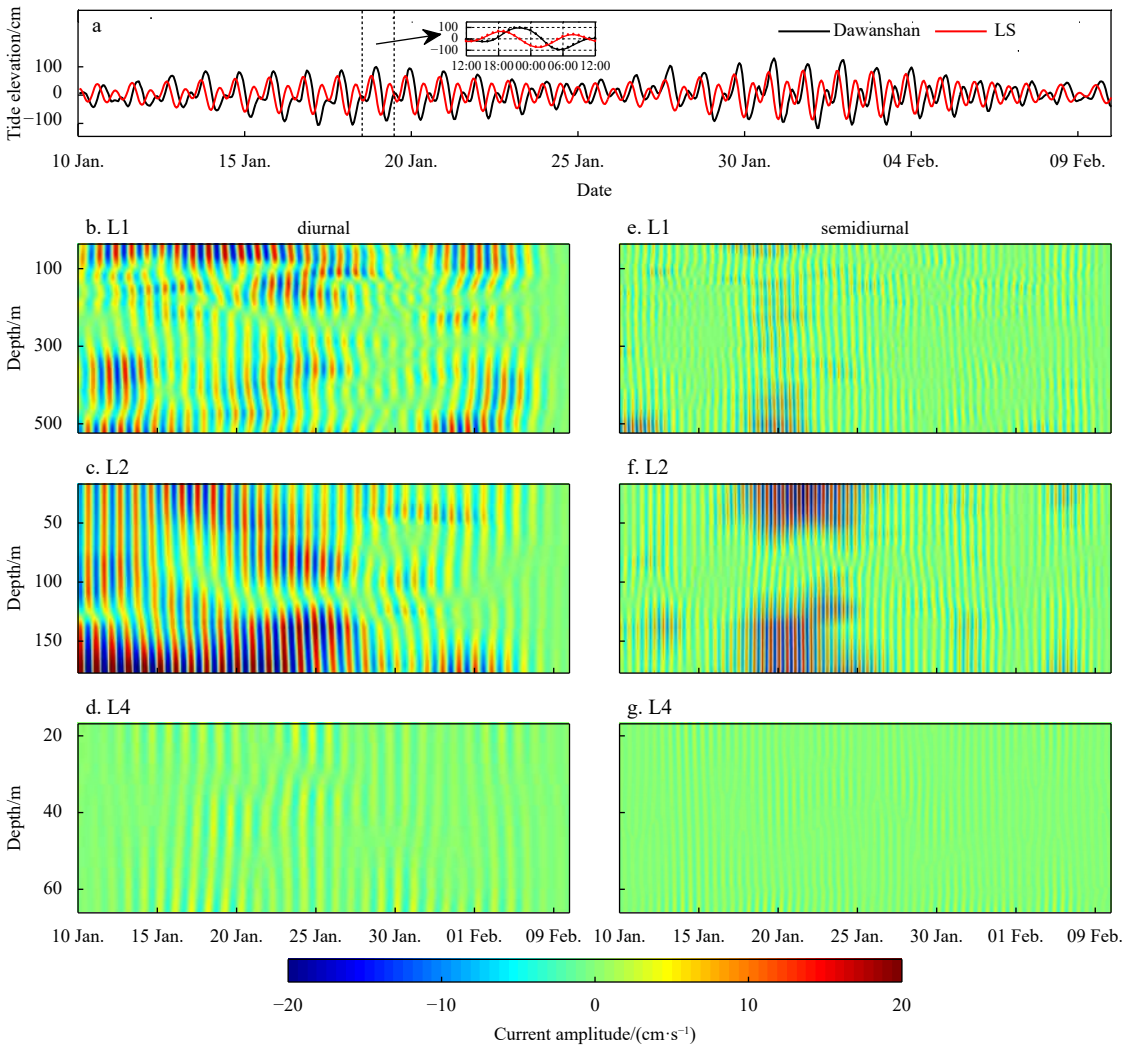


**Fig. 5.** Time series of tidal elevation at Dawanshan gauge station (black line) and the Luzon Strait (LS) (20°N, 122°E; red line) obtained from TPXO7.2 (a). Band-passed diurnal (b–d) and semidiurnal (e–g) baroclinic cross-shelf currents at L1, L2, and L4 from 10 January to 9 February 2018.

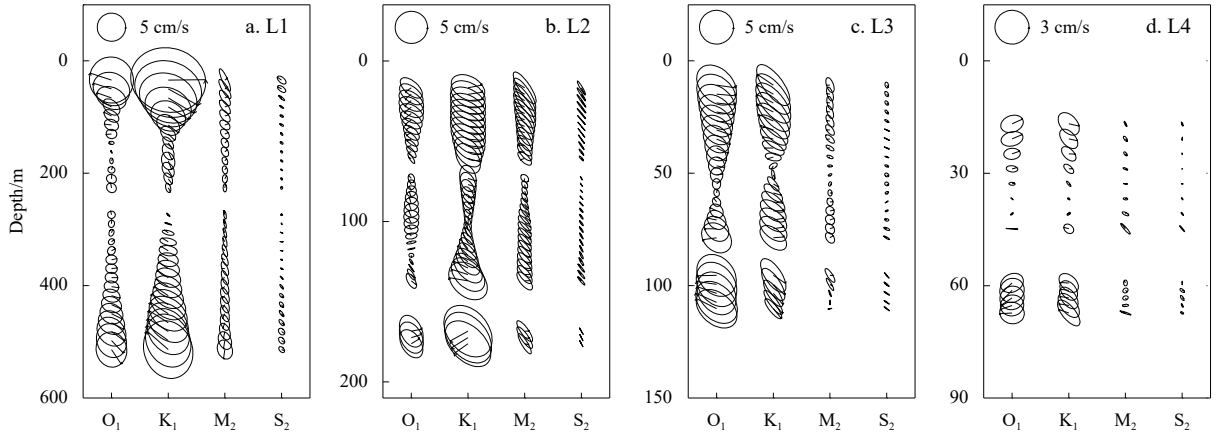


**Fig. 6.** Baroclinic tidal ellipses for the principal constituents ($O_1$, $K_1$, $M_2$ and $S_2$) at L1–L4. The ellipses are centered at the corresponding observed depth. The arrows denote the rotation direction of the ellipses, the lines from the center show the Greenwich phases, and the upper-left icon is the current scale for the axes.

cycle is still clear in summer, but gets ambiguous in winter (Fig. 7b). The averaged Mode-1 signal accounts for 70% of the total kinetic energy, and the Mode-2 and Mode-3 summed percentage is higher than the counterpart at L1, which may be related to the large energy dissipation from the slope to the continental shelf (Table 3). At L3, the averaged Mode-1 signal accounts for 82% of

the total energy, which is the highest among the four sites (Fig. 7c). Furthermore, the kinetic energy decreases by 31%, 64% and 66% for Mode-1, Mode-2 and Mode-3, respectively, when the diurnal ITs propagate from L2 to L3. At L4, the diurnal ITs only keep a certain intensity in summer (Fig. 7d) and the averaged Mode-1 accounts for 64% of the total kinetic energy (Table 3).

The semidiurnal ITs are also dominated by Mode-1 (Fig. 8), and the corresponding averaged Mode-1 signals account for 67%, 68%, 84% and 64% of the total kinetic energy (sum of the first three semidiurnal baroclinic modes, Table 3) at L1–L4. The Mode-2 and Mode-3 summed percentage, 40%, in winter is higher than the counterpart, 31%, in summer at L1. And the semidiurnal kinetic energy decreases by 42%, 79% and 69% for Mode-1, Mode-2 and Mode-3, respectively, when the semidiurnal ITs propagate from L2 to L3, which shows high-mode ITs are unstable and tend to dissipate quickly.

### 3.3.2 *Temporal and spatial variation of the total HKE*

By comparing the total HKE distribution of the first three baroclinic modes, the diurnal HKE is much larger than the semidiurnal HKE by a factor of 3–6 in summer and 2–4 in winter. The seasonal variation of HKE is not only related to the slope and shelf regions but also differs between diurnal and semidiurnal ITs. In the slope region west of the DP, diurnal ITs are stronger in summer and winter than in spring and autumn, which is especially obvious at L2. The seasonally averaged HKE of L2 is 1 136.1 J/m$^2$ in summer and 778.5 J/m$^2$ in winter, larger than the 374.2 J/m$^2$ in spring and 475.8 J/m$^2$ in autumn. At L1, the aver-

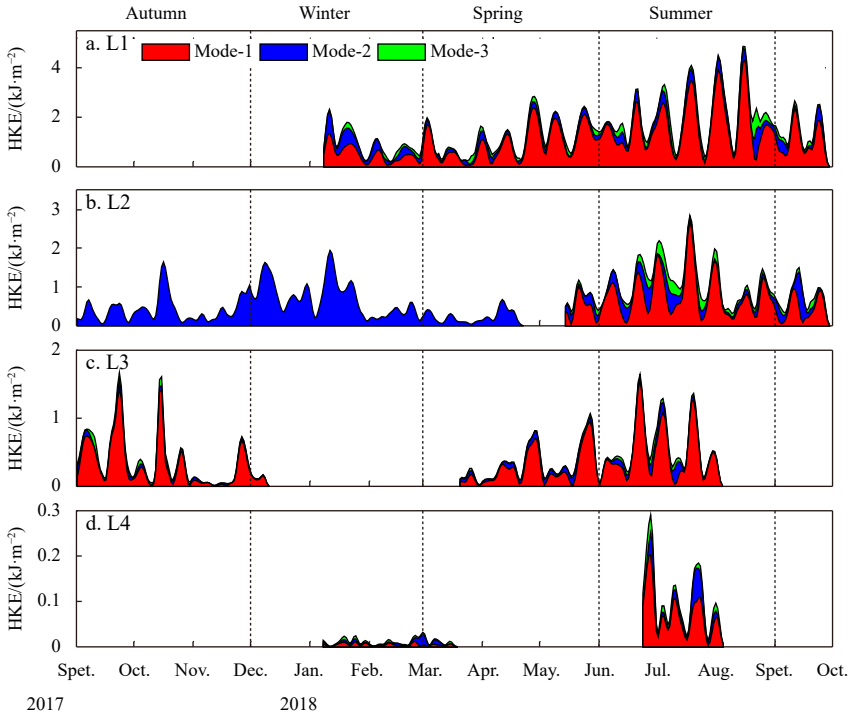


**Fig. 7.** Time series of Mode-1 (red), Mode-2 (blue), Mode-3 (green) diurnal horizontal kinetic energy (HKE) (kJ/m$^2$) at L1–L4 between September 2017 and October 2018.

**Table 3.** Time-averaged horizontal kinetic energy (HKE) (J/m$^2$) of the diurnal and semidiurnal internal tides at L1–L4

| | | Diurnal internal tide | | | | Semidiurnal internal tide | | | |
|---|---|---|---|---|---|---|---|---|---|
| | | Mode-1 | Mode-2 | Mode-3 | Total | Mode-1 | Mode-2 | Mode-3 | Total |
| L1 | Winter | 496.7 | 334.5 | 96.5 | 927.7 | 129.1 | 51.1 | 37.3 | 217.4 |
| | Spring | 922.5 | 160.6 | 99.3 | 1 182.4 | 211.3 | 54.7 | 35.5 | 301.5 |
| | Summer | 1 668.5 | 282.0 | 166.6 | 2 117.2 | 227.4 | 52.0 | 51.1 | 330.5 |
| | Observation | 1 109.2 | 245.5 | 124.4 | 1 479.1 | 202.3 | 59.4 | 41.7 | 303.4 |
| L2 | Autumn | 292.3 | 120.7 | 62.9 | 475.8 | 229.0 | 66.0 | 40.0 | 335.0 |
| | Winter | 621.2 | 82.8 | 74.6 | 778.5 | 284.3 | 91.8 | 35.4 | 411.6 |
| | Spring | 234.6 | 96.0 | 43.6 | 374.2 | 112.4 | 35.9 | 16.6 | 164.9 |
| | Summer | 808.1 | 193.5 | 134.5 | 1 136.1 | 220.5 | 82.0 | 30.6 | 333.1 |
| | Observation | 497.6 | 133.2 | 80.2 | 711.0 | 214.5 | 69.8 | 30.7 | 315.0 |
| L3 | Autumn | 328.9 | 37.5 | 31.7 | 398.2 | 139.9 | 15.7 | 12.7 | 168.4 |
| | Spring | 263.1 | 55.3 | 15.8 | 334.2 | 113.6 | 18.5 | 7.3 | 139.4 |
| | Summer | 481.4 | 61.5 | 37.5 | 580.3 | 127.3 | 11.4 | 8.8 | 147.5 |
| | Observation | 340.8 | 48.2 | 27.3 | 416.2 | 125.2 | 14.9 | 9.7 | 149.8 |
| L4 | Winter | 4.5 | 3.6 | 2.6 | 10.7 | 1.3 | 0.7 | 0.7 | 2.8 |
| | Summer | 69.5 | 20.1 | 12.1 | 101.6 | 14.1 | 2.8 | 3.0 | 19.9 |
| | Observation | 28.8 | 10.2 | 6.1 | 45.1 | 6.3 | 1.7 | 1.8 | 9.8 |

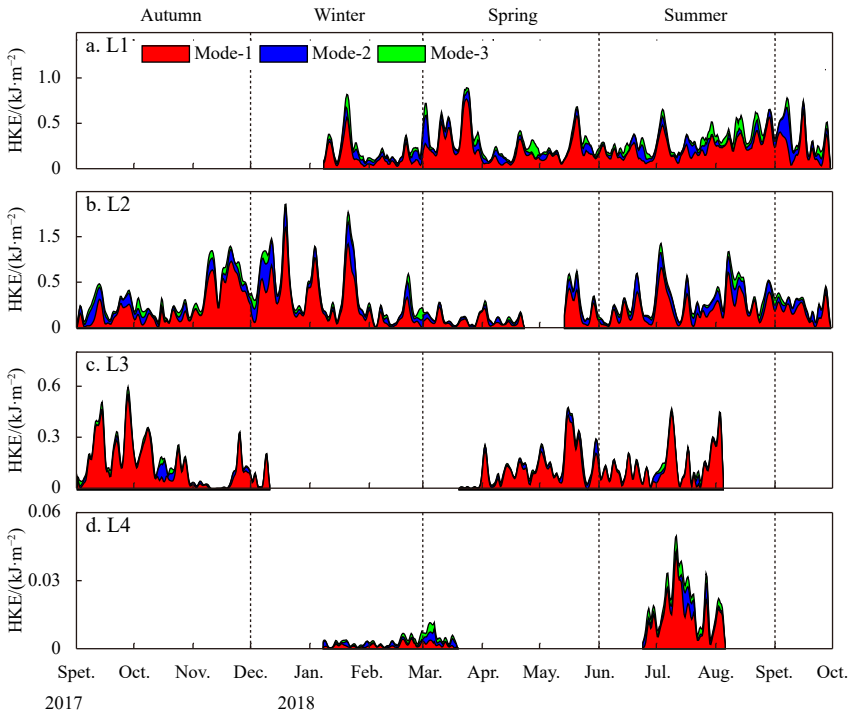


**Fig. 8.** Time series of Mode-1 (red), Mode-2 (blue), Mode-3 (green) semidiarnal horizontal kinetic energy (HKE) (kJ/m²) at L1–L4 between September 2017 and October 2018.

aged HKE in summer is 2 117.2 J/m², which is the maximum for all four sites, although the averaged HKE of 1 182.4 J/m² in spring is a little larger than that in winter, but this may be related to the missing data in December 2017. The diurnal HKE is stronger in summer at L3, but note that the intensity of diurnal ITs during the stronger spring-neap cycle in autumn is comparable with that in summer. Both diurnal and semidiurnal ITs maintain a certain intensity in summer but almost disappear in winter at L4. The HKE of semidiurnal ITs also shows a similar seasonal variation, with semidiurnal ITs being stronger around summer and winter at L1 and L2. Unlike diurnal ITs, the semidiurnal HKE is even stronger in winter than in summer.

## 4 Discussion

### 4.1 *Ocean stratification and tide modulation*

The northern SCS is under the influence of the East Asian monsoon system (Su, 2004), accompanied by complex dynamic processes, such as the Kuroshio intrusion (Xue et al., 2004), mesoscale eddies (Xiu et al., 2010; Wang et al., 2003), and fresh water plume and coastal upwelling (Gan et al., 2009); therefore upper-ocean stratification changes greatly with the season.

There are obvious seasonal variations of stratification in the upper water column (Fig. 9). Variations in temperature ($T$) and salinity ($S$) at S1 are concentrated mainly in the upper 100 m; the maximum buoyancy frequency reaches the shallowest depth of ~45 m in summer (August 2017), and the deepest depth of ~100 m in winter (January 2018, Fig. 2a). Compared to S1, even greater thermocline depth variation is found at S2, where the mixed layer depth is less than 20 m in summer and reaches ~80 m in winter (Fig. 2b). S3 and S4 are located on the shallow shelf outside of the ZRE, and the $T$, $S$ and $N$ are completely mixed in winter but exhibit apparent stratifications in summer (Figs 2c and d). Therefore, seasonal stratification variation in the slope-shelf area west of the DP is confined mainly in the upper 100 m. The reversal depth of the baroclinic $K_1$ tidal ellipse is ~270 m at L1. For the slope area with deep water, the influence of stratification on ITs may be limited. However, for the shallow shelf area, since stratification is maintained in summer under the effect of solar radiation and the fresh water plume but it almost disappears in winter, its impact on ITs may be decisive.

Diurnal ITs are also stronger in winter and summer in the southern SCS (Shang et al., 2015) and western SCS (Zhai et al., 2020), and the barotropic tidal input from the LS is considered to be the main influencing factor. Barotropic current amplitudes of principal diurnal constituents obtained from TPXO7.2 show a semi-annual cycle with the greatest current magnitudes close to 30 cm/s, while there is no obvious seasonal variation for the principal semidiurnal tides with current amplitudes of less than 20 cm/s (Fig. 10a). Shang et al. (2015) also pointed out that the modulation of $K_1$ and $P_1$ accounted for this semi-annual cycle of diurnal barotropic currents. We further present daily averaged water level at Dawanshan gauge station, which also shows stronger tidal energy in summer and winter, and the peak value in September 2018 is induced by super typhoon Mangkhut (Fig. 10b).

In summary, seasonal variation of stratification in the slope area west of the DP is concentrated mainly in the upper water column, and the corresponding influences on the structure and propagation of ITs are limited. The temporal variation of diurnal ITs is determined by barotropic tidal input from the LS. In contrast, for the shallow shelf area, the strength of ITs is heavily influenced by seasonal stratification, although there is still strong tidal energy input in winter, and baroclinic energy rapidly dissipates during cross-shelf propagation as the water column is almost completely mixed in the vertical.

### 4.2 *Coherent and incoherent variation*

To quantify the coherent and incoherent features at the four moorings, time series of current variances (Var= $u^2+v^2$) for both

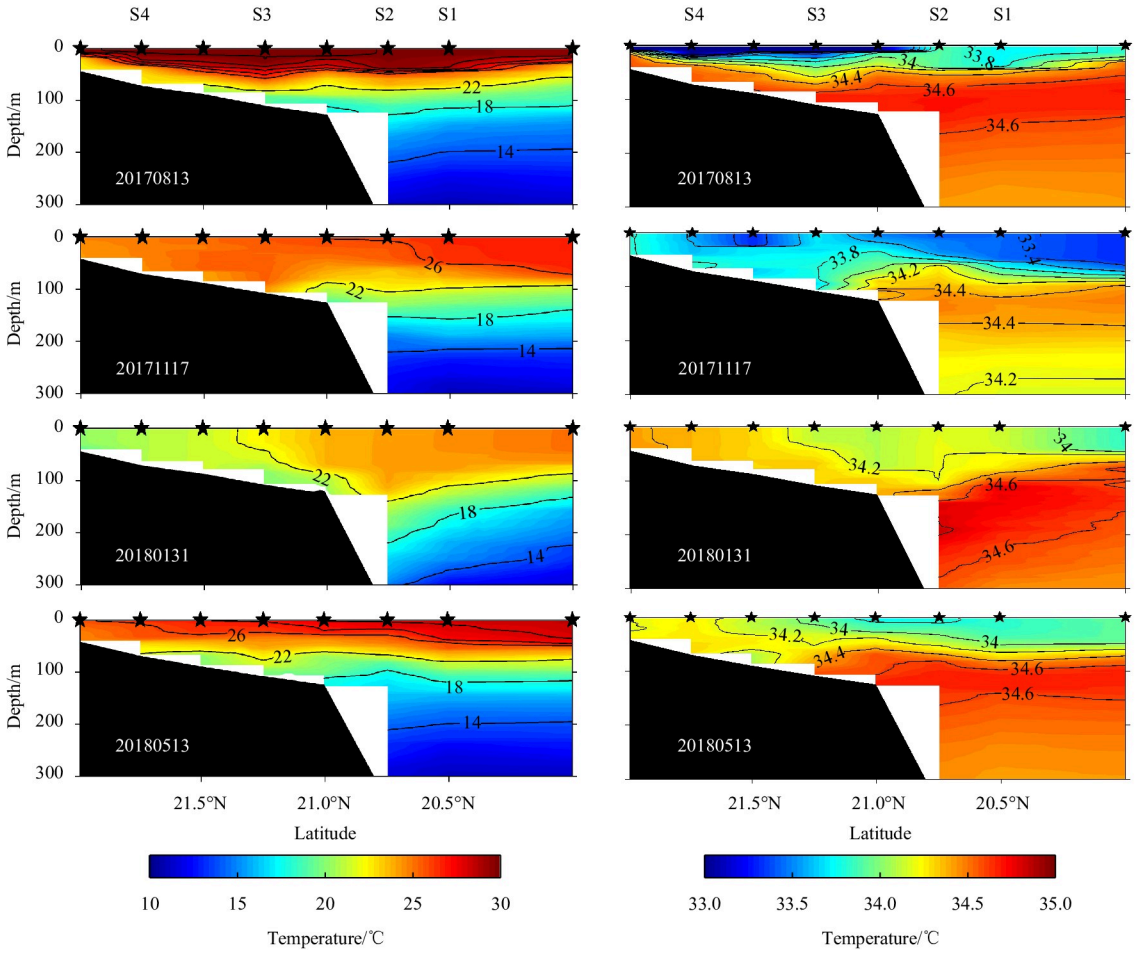


**Fig. 9.** Temperature (*T*) and salinity (*S*) distribution of the hydrological section west of the Dongsha Plateau in different seasons, black stars are the CTD stations, and S1–S4 are indicated. Date format is YYYY.MM.DD.

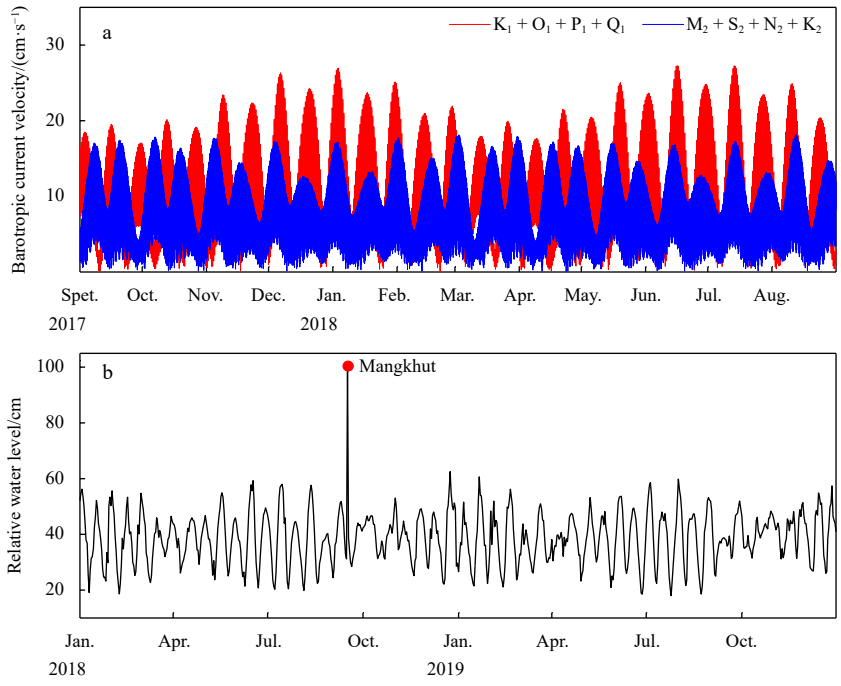


**Fig. 10.** Time series of principal diurnal (red) and semidiurnal (blue) barotropic currents obtained from TPXO7.2 at Luzon Strait (20°N, 122°E) (a) and observed daily averaged water level at Dawanshan station (relative to the local tide datum) (b).

coherent and incoherent ITs are presented (Fig. 11). For diurnal ITs at L1 and L2, the coherent current variances are stronger in winter and summer, but weaker in spring and autumn, and they also show a pronounced fortnightly spring-neap cycle, whereas the incoherent motions display an irregular seasonal variation and show intermittent maximum values. Moreover, the coherent portions are stronger than their incoherent counterparts. At L3 the coherent motions are strong in summer, but the incoherent portions dominate in the other seasons, and the proportion of incoherent motions are further increased at L4. The coherent diurnal baroclinic current variances account for 58.9%, 56.3%, 52.5%, and 38.9% of diurnal ITs at L1–L4, showing a decreasing trend along the cross-shelf direction, and the corresponding ratios are only 33.9%, 42.9%, 20.1% and 34.5% for semidiurnal ITs at L1–L4, which indicates strong incoherent features.

The coherent variances explain ~90% of diurnal ITs in the southern portion of the LS (Xu et al., 2014), and ~74% in the northern SCS deep basin (Li et al., 2020), then decrease to ~60% in the slope area around the DP (Xu et al., 2013; Cao et al., 2017) and ~17.5% in the shelf area outside of the ZRE (Jiang et al., 2019). For semidiurnal ITs, the coherent variances explain ~65% in the LS (Xu et al., 2014), and 61% in the adjacent deep basin (Li et al., 2020), then largely decrease to 10%–30% in the slope-shelf area around the DP (Xu et al., 2013; Jiang et al., 2019). Based on these previous studies and the results in this paper, we find that diurnal ITs are more coherent than semidiurnal ITs in the northern SCS, and the coherent signals are stronger than their incoherent counterparts for diurnal ITs. For the diurnal ITs, the ratio of coherent variances reaches ~60% in the slope area west of the DP, while for semidiurnal ITs the baroclinic currents are dominated by the incoherent portions over the slope-shelf area in the northern SCS. As such the semidiurnal ITs don't have apparent seasonal variation because as the main contributor the incoherent motions have no regular seasonal variation. Since seafloor inclination is near critical for diurnal ITs (Duda and Rainville, 2008), and numerical study further shows ~1.6 GW $K_1$, ITs generated in the slope area around the DP which is nearly twice of $M_2$ ITs (Xu et al., 2016), the locally generated diurnal ITs may strengthen the coherent nature, while numerical studies show that semidiurnal ITs in the northern SCS are more sensitive to the influence of background dynamic processes to become more incoherent than diurnal ITs (Li et al., 2020).

## 5 Summary

Current observations from 4 near-full-depth moorings are collected to characterize ITs in the slope-shelf area west of the DP, and these four ADCP moorings also capture the cross-shelf variations of ITs. Diurnal ITs dominate over semidiurnal ITs in

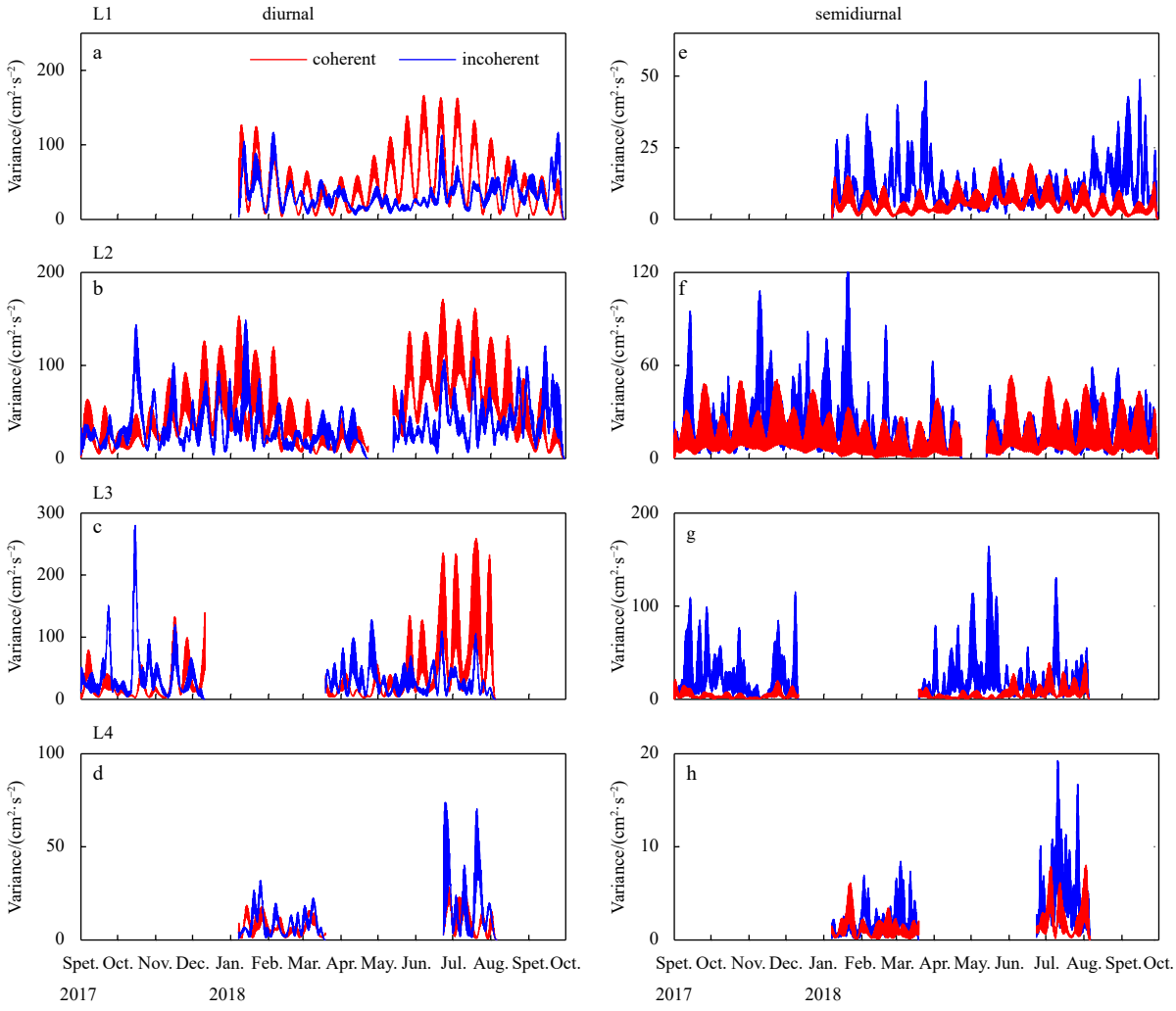


**Fig. 11.** Time series of the coherent and incoherent diurnal (a–d) and semidiurnal (e–h) baroclinic current variances ($cm^2/s^2$) averaged in the vertical direction at L1–L4.

the slope region, and the amplitudes of diurnal baroclinic currents can be more than 5 times larger than those of barotropic currents. When ITs propagate from the slope to the shelf region, baroclinic energy quickly dissipates. Meanwhile, high baroclinic mode structures might appear. The amplitudes of baroclinic currents decrease and the amplitudes of barotropic currents increase. On the shallow shelf outside of the ZRE, the barotropic currents become dominant with the amplitudes of semidiurnal barotropic currents being 10 times more than those of the baroclinic ones.

The first baroclinic mode is dominant for both diurnal and semidiurnal ITs throughout the whole observation period. Based on a 9-month ADCP data set collected on the slope region west of the DP, Xu et al. (2013) emphasized that semidiurnal ITs showed a seasonal multimodal structure, and Mode-2 was dominant in summer. However, the modal decomposition results in this paper indicate that there is no clear seasonal multimodal structure, the percent of high-mode signals tend to increase as the ITs propagate from the continental slope to the shelf, but these ITs are unstable and dissipated quickly, hence short lived for less than 3 d, just like the duration of the Mode-2 diurnal and semidiurnal ITs observed at L2 and L1 in this study and those reported by Xu et al. (2013).

Seasonal variation of ITs in the northern SCS has been widely investigated, but as an important supplement, this paper for the first time comprehensively presents the characteristics and cross-shelf variations of ITs in the slope-shelf area west of the DP. By summarizing all these studies, we can see that from the LS to the slope region in the northern SCS, diurnal ITs show an apparent seasonally dependent variation, being stronger in summer and winter but weaker in spring and autumn, whereas the semidiurnal ITs are seasonally independent. Diurnal ITs are controlled by the semi-annual cycle of barotropic energy input from the LS, while the dominant incoherent motions account for the irregular seasonal variation of semidiurnal ITs. For the shallow shelf region, both diurnal and semidiurnal ITs maintain a certain intensity in summer but almost disappear in winter. There is still strong barotropic energy input in winter, but baroclinic energy largely dissipates during the onshore propagation when the water column is completely mixed on the shallow shelf in winter.

***Acknowledgements***

We appreciate the captain and crew for their hard work in collecting mooring data during the in-field cruises. We also thank two anonymous reviewers for helpful comments and suggestions which improved this work.

**References**

Alford M H. 2003. Redistribution of energy available for ocean mixing by long-range propagation of internal waves. Nature, 423(6936): 159–162, doi: 10.1038/nature01628

Alford M H, MacKinnon J A, Nash J D, et al. 2011. Energy flux and dissipation in Luzon Strait: two tales of two ridges. Journal of Physical Oceanography, 41(11): 2211–2222, doi: 10.1175/JPO-D-11-073.1

Alford M H, Peacock T, MacKinnon J A, et al. 2015. The formation and fate of internal waves in the South China Sea. Nature, 521(7550): 65–69, doi: 10.1038/nature14399

Beardsley R C, Duda T F, Lynch J F, et al. 2004. Barotropic tide in the northeast South China Sea. IEEE Journal of Oceanic Engineering, 29(4): 1075–1086, doi: 10.1109/joe.2004.833226

Cao Anzhou, Guo Zheng, Lv Xianqing, et al. 2017. Coherent and incoherent features, seasonal behaviors and spatial variations of internal tides in the northern South China Sea. Journal of Marine Systems, 172: 75–83, doi: 10.1016/j.jmarsys.2017.03.005

Chen Shengli, Chen Daoyi, Xing Jiuxing, et al. 2019. Features of internal tides observed near the shelf break in the northern South China Sea. Ocean Dynamics, 69(3): 353–365, doi: 10.1007/s10236-019-01248-4

Duda T F, Lynch J F, Irish J D, et al. 2004. Internal tide and nonlinear internal wave behavior at the continental slope in the northern South China Sea. IEEE Journal of Oceanic Engineering, 29(4): 1105–1130, doi: 10.1109/joe.2004.836998

Duda T F, Rainville L. 2008. Diurnal and semidiurnal internal tide energy flux at a continental slope in the South China Sea. Journal of Geophysical Research: Oceans, 113(C3): C03025, doi: 10.1029/2007JC004418

Egbert G D, Erofeeva S Y. 2002. Efficient inverse modeling of barotropic ocean tides. Journal of Atmospheric and Oceanic Technology, 19(2): 183–204, doi: 10.1175/1520-0426(2002)019<0183:EIMOBO>2.0.CO;2

Eich M L, Merrifield M A, Alford M H. 2004. Structure and variability of semidiurnal internal tides in Mamala Bay, Hawaii. Journal of Geophysical Research: Oceans, 109(C5): C05010, doi: 10.1029/2003JC002049

Fang Guohong, Kwok Y K, Yu Kejun, et al. 1999. Numerical simulation of principal tidal constituents in the South China Sea, Gulf of Tonkin and Gulf of Thailand. Continental Shelf Research, 19(7): 845–869, doi: 10.1016/s0278-4343(99)00002-3

Farmer D, Li Qiang, Park J H. 2009. Internal wave observations in the South China Sea: the role of rotation and non-linearity. Atmosphere-Ocean, 47(4): 267–280, doi: 10.3137/OC313.2009

Gan Jianping, Li Li, Wang Dongxiao, et al. 2009. Interaction of a river plume with coastal upwelling in the northeastern South China Sea. Continental Shelf Research, 29(4): 728–740, doi: 10.1016/j.csr.2008.12.002

Garrett C, Kunze E. 2007. Internal tide generation in the deep ocean. Annual Review of Fluid Mechanics, 39: 57–87, doi: 10.1146/annurev.fluid.39.050905.110227

Gill A E. 1982. Atmosphere-Ocean Dynamics. New York: Academic Press

Guo Pu, Fang Wendong, Liu Changjian, et al. 2012. Seasonal characteristics of internal tides on the continental shelf in the northern South China Sea. Journal of Geophysical Research: Oceans, 117(C4): C04023, doi: 10.1029/2011JC007215

Holloway P E, Chatwin P G, Craig P. 2001. Internal tide observations from the Australian North West shelf in Summer 1995. Journal of Physical Oceanography, 31(5): 1182–1199, doi: 10.1175/1520-0485(2001)031<1182:ITOFTA>2.0.CO;2

Huang Xiaodong, Wang Zhaoyun, Zhang Zhiwei, et al. 2018. Role of mesoscale eddies in modulating the semidiurnal internal tide: observation results in the northern South China Sea. Journal of Physical Oceanography, 48(8): 1749–1770, doi: 10.1175/JPO-D-17-0209.1

Jan Sen, Chern Ching-Sheng, Wang Joe, et al. 2007. Generation of diurnal $K_1$ internal tide in the Luzon Strait and its influence on surface tide in the South China Sea. Journal of Geophysical Research: Oceans, 112(C6): C06019, doi: 10.1029/2006JC004003

Jan Sen, Lien Ren-Chieh, Ting Chihua. 2008. Numerical study of baroclinic tides in Luzon Strait. Journal of Oceanography, 64(5): 789–802, doi: 10.1007/s10872-008-0066-5

Jiang Shumin, Dai Dejun, Qiao Fangli, et al. 2019. The internal tides on continental shelf of the northern South China Sea. Oceanologia et Limnologia Sinica (in Chinese), 50(1): 1–11, doi: 10.11693/hyhz20180300046

Kelly S M, Nash J D, Martini K I, et al. 2012. The cascade of tidal energy from low to high modes on a continental slope. Journal of Physical Oceanography, 42(7): 1217–1232, doi: 10.1175/JPO-D-11-0231.1

Klymak J M, Alford M H, Pinkel R, et al. 2011. The breaking and scattering of the internal tide on a continental slope. Journal of Physical Oceanography, 41(5): 926–945, doi: 10.1175/2010JPO4500.1

Li Bingtian, Wei Zexun, Wang Xinyi, et al. 2020. Variability of coherent and incoherent features of internal tides in the north South China Sea. Scientific Reports, 10(1): 12904, doi: 10.1038/s41598-

020-68359-7
Lien Ren-Chiel, Tang Tswen Yung, Chang Ming-Huei, et al. 2005. Energy of nonlinear internal waves in the South China Sea. Geophysical Research Letters, 32(5): L05615, doi: 10.1029/2004GL022012
Liu Junliang, He Yinghui, Wang Dongxiao, et al. 2015. Observed enhanced internal tides in winter near the Luzon Strait. Journal of Geophysical Research: Oceans, 120(10): 6637–6652, doi: 10.1002/2015JC011131
Liu Qian, Xie Xiaohui, Shang Xiaodong, et al. 2016. Coherent and incoherent internal tides in the southern South China Sea. Chinese Journal of Oceanology and Limnology, 34(6): 1374–1382, doi: 10.1007/s00343-016-5171-5
Liu Qian, Xie Xiaohui, Shang Xiaodong, et al. 2019. Modal structure and propagation of internal tides in the northeastern South China Sea. Acta Oceanologica Sinica, 38(9): 12–23, doi: 10.1007/s13131-019-1473-1
Ma Barry B, Lien Ren-Chiel, Ko Dong S. 2013. The variability of internal tides in the northern South China Sea. Journal of Oceanography, 69(5): 619–630, doi: 10.1007/s10872-013-0198-0
Nash J D, Alford M H, Kunze E. 2005. Estimating internal wave energy fluxes in the ocean. Journal of Atmospheric and Oceanic Technology, 22(10): 1551–1570, doi: 10.1175/JTECH1784.1
Niwa Y, Hibiya T. 2001. Numerical study of the spatial distribution of the $M_2$ internal tide in the Pacific Ocean. Journal of Geophysical Research: Oceans, 106(C10): 22441–22449, doi: 10.1029/2000JC000770
Niwa Y, Hibiya T. 2004. Three-dimensional numerical simulation of $M_2$ internal tides in the East China Sea. Journal of Geophysical Research: Oceans, 109(C4): C04027, doi: 10.1029/2003JC001923
Park J H, Andres M, Martin P J, et al. 2006. Second-mode internal tides in the East China Sea deduced from historical hydrocasts and a model. Geophysical Research Letters, 33(5): L05602, doi: 10.1029/2005GL024732
Pawlowicz R, Beardsley B, Lentz S. 2002. Classical tidal harmonic analysis including error estimates in MATLAB using T_TIDE. Computers & Geosciences, 28(8): 929–937, doi: 10.1016/S0098-3004(02)00013-4
Rainville L, Pinkel R. 2006. Propagation of low-mode internal waves through the ocean. Journal of Physical Oceanography, 36(6): 1220–1236, doi: 10.1175/JPO2889.1
Ramp S R, Tang T Y, Duda T F, et al. 2004. Internal solitons in the northeastern South China Sea. Part I: sources and deep water propagation. IEEE Journal of Oceanic Engineering, 29(4): 1157–1181, doi: 10.1109/JOE.2004.840839
Shang Xiaodong, Liu Qian, Xie Xiaohui, et al. 2015. Characteristics and seasonal variability of internal tides in the southern South China Sea. Deep-Sea Research Part I: Oceanographic Research Papers, 98: 43–52, doi: 10.1016/j.dsr.2014.12.005
St. Laurent L, Garrett C. 2002. The role of internal tides in mixing the deep ocean. Journal of Physical Oceanography, 32(10): 2882–2899, doi: 10.1175/1520-0485(2002)032<2882:TROITI>2.0.CO;2
Su Jilan. 2004. Overview of the South China Sea circulation and its influence on the coastal physical oceanography outside the Pearl River Estuary. Continental Shelf Research, 24(16): 1745–1760, doi: 10.1016/j.csr.2004.06.005
Subeesh M P, Unnikrishnan A S. 2016. Observed internal tides and near-inertial waves on the continental shelf and slope off Jaigarh, central west coast of India. Journal of Marine Systems, 157: 1–19, doi: 10.1016/j.jmarsys.2015.12.005
Tian Jiwei, Yang Qingxuan, Zhao Wei. 2009. Enhanced diapycnal mixing in the South China Sea. Journal of Physical Oceanography, 39(12): 3191–3203, doi: 10.1175/2009JPO3899.1
Tian Jiwei, Zhou Lei, Zhang Xiaoqian. 2006. Latitudinal distribution of mixing rate caused by the $M_2$ internal tide. Journal of Physical Oceanography, 36(1): 35–42, doi: 10.1175/JPO2824.1
van Haren H. 2004. Incoherent internal tidal currents in the deep ocean. Ocean Dynamics, 54(1): 66–76, doi: 10.1007/s10236-003-0083-2
Wang Guihua, Su Jilan, Chu Peter C. 2003. Mesoscale eddies in the South China Sea observed with altimeter data. Geophysical Research Letters, 30(21): 2121, doi: 10.1029/2003GL018532
Xie Xiaohui, Liu Qian, Zhao Zhongxiang, et al. 2018. Deep sea currents driven by breaking internal tides on the continental slope. Geophysical Research Letters, 45(12): 6160–6166, doi: 10.1029/2018GL078372
Xie Xiaohui, Shang Xiaodong, van Haren H, et al. 2013. Observations of enhanced nonlinear instability in the surface reflection of internal tides. Geophysical Research Letters, 40(8): 1580–1586, doi: 10.1002/grl.50322
Xiu Peng, Chai Fei, Shi Lei, et al. 2010. A census of eddy activities in the South China Sea during 1993–2007. Journal of Geophysical Research: Oceans, 115(C3): C03012, doi: 10.1029/2009JC005657
Xu Zhenhua, Liu Kun, Yin Baoshu, et al. 2016. Long-range propagation and associated variability of internal tides in the South China Sea. Journal of Geophysical Research: Oceans, 121(11): 8268–8286, doi: 10.1002/2016JC012105
Xu Zhenhua, Wang Yang, Liu Zhiqiang, et al. 2021. Insight into the dynamics of the radiating internal tide associated with the Kuroshio Current. Journal of Geophysical Research: Oceans, 126(6): e2020JC017018, doi: 10.1029/2020JC017018
Xu Zhenhua, Yin Baoshu, Hou Yijun, et al. 2013. Variability of internal tides and near-inertial waves on the continental slope of the northwestern South China Sea. Journal of Geophysical Research: Oceans, 118(1): 197–211, doi: 10.1029/2012JC008212
Xu Zhenhua, Yin Baoshu, Hou Yijun, et al. 2014. Seasonal variability and north–south asymmetry of internal tides in the deep basin west of the Luzon Strait. Journal of Marine Systems, 134: 101–112, doi: 10.1016/j.jmarsys.2014.03.002
Xue Huijie, Chai Fei, Pettigrew N, et al. 2004. Kuroshio intrusion and the circulation in the South China Sea. Journal of Geophysical Research: Oceans, 109(C2): C02017, doi: 10.1029/2002JC001724
Zhai Rongwei, Chen Guiying, Liang Changrong, et al. 2020. The influence of ENSO on the structure of internal tides in the Xisha Area. Journal of Geophysical Research: Oceans, 125(3): e2019JC015405, doi: 10.1029/2019JC015405
Zhao Zhongxiang. 2014. Internal tide radiation from the Luzon Strait. Journal of Geophysical Research: Oceans, 119(8): 5434–5448, doi: 10.1002/2014JC010014
Zhao Zhongxiang, Alford M H, MacKinnon J A, et al. 2010. Long-range propagation of the semidiurnal internal tide from the Hawaiian Ridge. Journal of Physical Oceanography, 40(4): 713–736, doi: 10.1175/2009JPO4207.1
Zu Tingting, Gan Jianping, Erofeeva S Y. 2008. Numerical study of the tide and tidal dynamics in the South China Sea. Deep-Sea Research Part I: Oceanographic Research Papers, 55(2): 137–154, doi: 10.1016/j.dsr.2007.10.007